
BLENDENET++: A LARGE-SCALE BLENDED WING BODY AERODYNAMICS DATASET AND BENCHMARK

Nicholas Sung*

Department of Mechanical Engineering
Massachusetts Institute of Technology
Cambridge, MA
nicksung@mit.edu

Steven Spreizer*

MIT Lincoln Laboratory
Lexington, MA
steven.spreizer@ll.mit.edu

Mohamed Elrefaie

Department of Mechanical Engineering
Massachusetts Institute of Technology
Cambridge, MA
mohamed.elrefaie@mit.edu

Matthew C. Jones

MIT Lincoln Laboratory
Lexington, MA
matthew.jones@ll.mit.edu

Faez Ahmed

Department of Mechanical Engineering
Massachusetts Institute of Technology
Cambridge, MA
faez@mit.edu

ABSTRACT

Despite progress in machine learning based aerodynamic surrogates, the scarcity of large, field-resolved datasets limits progress on accurate pointwise prediction and reproducible inverse design for aircraft. We introduce **BlendedNet++**, a large-scale aerodynamic dataset and benchmark focused on blended wing body (BWB) aircraft. The dataset contains over 12,000 unique geometries, each simulated at a single flight condition, yielding **12,490** aerodynamic results for steady RANS CFD. For every case, we provide (i) integrated force/moment coefficients C_L , C_D , C_M and (ii) dense surface fields of pressure and skin friction coefficients — C_p and $(C_{f_x}, C_{f_y}, C_{f_z})$. Using this dataset, we standardize a forward-surrogate benchmark to predict pointwise fields across six model families: *GraphSAGE*, *GraphUNet*, *PointNet*, a coordinate *Transformer* (Transolver-style), a *FiLMNet* (coordinate MLP with feature-wise modulation), and a *Graph Neural Operator Transformer* (GNOT). Finally, we present an inverse design task of achieving a specified lift-to-drag ratio under fixed flight conditions, implemented via a *conditional diffusion* model. To assess performance, we benchmark this approach against gradient-based optimization on the same surrogate and a diffusion–optimization hybrid that first samples with the conditional diffusion model and then further optimizes the designs.

BlendedNet++ provides a unified forward and inverse protocol with multi-model baselines, enabling fair, reproducible comparison across architectures and optimization paradigms. We expect BlendedNet++ to catalyze reproducible research in field-level aerodynamics and inverse design; resources (dataset, splits, baselines, and scripts) will be released upon acceptance.

Keywords Blended Wing Body · Aerodynamics Dataset · Surrogate Modeling · Inverse Design · Conditional Diffusion

*These authors contributed equally to this work.

Nomenclature

(All symbols include units where applicable; “–” denotes dimensionless.)

Aerodynamic Coefficients

C_L	= lift coefficient [–]
C_D	= drag coefficient [–]
C_M	= pitching-moment coefficient about nose reference [–]
C_p	= surface pressure coefficient [–]
C_{f_x}	= skin-friction coefficient, streamwise component [–]
C_{f_y}	= skin-friction coefficient, spanwise component [–]
C_{f_z}	= skin-friction coefficient, vertical component [–]
L/D	= lift-to-drag ratio [–]

Geometry and Coordinates

$x = (x, y, z)$	= Cartesian coordinates on surface mesh [m]
$n = (n_x, n_y, n_z)$	= outward unit surface normal [–]
C_1	= centerline length (reference length) [m]
C_2, C_3, C_4	= chord lengths at planform stations [m]
$C_2/C_1, C_3/C_1, C_4/C_1$	= chord-length ratios (station-to-centerline) [–]
B_1, B_2, B_3	= spanwise station locations measured from centerline [m]
$B_1/C_1, B_2/C_1, B_3/C_1$	= span-fraction parameters [–]
X_3	= streamwise location of outboard break [m]
S_1, S_3	= inboard / outboard leading-edge sweep angles [deg]
y^+	= non-dimensional wall distance [–]

Flight Conditions

alt_{kft}	= altitude [kft]
M_∞	= free-stream Mach number [–]
Re_L	= Reynolds number based on $L = C_1$ [–]
α	= angle of attack [deg]

Learning / Inference Variables

$p \in \mathbb{R}^9$	= planform parameter vector ($B_1/C_1, B_2/C_1, B_3/C_1, C_2/C_1, C_3/C_1, C_4/C_1, S_1, S_3, X_3/C_1$)
μ	= conditioning vector for inverse design ($\text{alt}_{\text{kft}}, \log_{10} Re_L, M_\infty, \alpha, (L/D)_{\text{target}}$)

1 Introduction

Blended Wing Body (BWB) aircraft have gained significant attention as a promising next-generation configuration due to their potential for enhanced aerodynamic efficiency and fuel economy. By integrating the fuselage and wings into a single lifting surface, BWBs can achieve higher lift-to-drag ratios, reduced structural weight, and lower fuel consumption relative to conventional tube-and-wing designs [1]. Early studies and recent assessments corroborate these advantages, reporting sizable reductions in fuel burn alongside structural benefits [1–3]. Realizing these gains, however, demands accurate modeling of complex aerodynamics. High-fidelity CFD is a natural fit but remains computationally intensive for large design sweeps, slowing concept iteration and constraining broad design-of-experiments [4, 5].

Why machine learning? Data-driven surrogates can approximate high-fidelity solvers at orders-of-magnitude lower runtime, enabling rapid screening, sensitivity analysis, and inverse design under tight iteration budgets [6, 7]. Yet surrogates trained on small or narrow datasets tend to overfit specific geometries or flight conditions and fail to generalize. This challenge is amplified for *field-level* prediction, where learning dense surface quantities (C_p, C_f) is high-dimensional and requires many *unique* shapes with consistent labels to capture local boundary-layer behavior and nonlocal interactions across the airframe. Empirically, recent field-resolved works in external aerodynamics (e.g., *DrivAerNet++*) show that scaling both dataset size and physical fidelity systematically improves predictive accuracy and out-of-distribution robustness, and reveals clear scaling behaviors in aerodynamic learning tasks [8–10]. Robust surrogates therefore require large, diverse, field-resolved datasets with standardized splits and metrics for fair assessment and reproducibility. Because architectures encode different inductive biases such as point set, graph, transformer/operator, and FiLM style conditioning, robust conclusions require a standardized benchmark across model families. We evaluate six complementary families on a shared, geometry-disjoint split to compare accuracy and scalability on equal footing.

BlendedNet² [11] took an initial step toward addressing data scarcity with 1099 geometries and dense surface outputs across multiple flight conditions, demonstrating that data-driven surrogates can predict pointwise pressure and skin-friction fields with low error. Yet, broader exploration of BWB design still lacks (i) a larger, more realistic design space with tighter parameter bounds, (ii) standardized, geometry-disjoint splits and consistent forward benchmarks across diverse machine learning model families, and (iii) a clear, reproducible inverse-design baseline using generative AI beyond purely gradient-based surrogates.

BlendedNet++ expands this line: 12,490 distinct BWB geometries at one flight condition each, all with integrated coefficients and dense surface fields. We (1) document an updated, planform-centric parameterization with realistic bounds inspired by prior work [12] and multi-fidelity practice [13–15]; (2) release geometry-disjoint splits; (3) establish a six-model forward benchmark spanning graph, point-set, coordinate-transformer, FiLM, and operator-learning paradigms; and (4) compare a conditional diffusion model, a gradient-based optimizer, and a diffusion–optimization hybrid that first samples diverse candidates with the conditional diffusion model and then locally optimizes them for near-exact target lift to drag adherence.

Our contributions are the following:

- **Scaled BWB dataset with surface fields.** 12,490 geometries (one flight condition each) with C_L , C_D , C_M and dense surface C_p , $(C_{f_x}, C_{f_y}, C_{f_z})$, enabling field-level learning at scale.
- **Realistic parameterization and standardized splits.** Updated bounds and geometry-disjoint train/test splits for fair comparison and robust generalization.
- **Six-family forward benchmark.** GraphSAGE, GraphUNet, PointNet, a coordinate Transformer (Transolver-style), FiLMNet, and a Graph Neural Operator Transformer (GNOT) with unified metrics on pointwise fields.
- **Inverse-design baseline.** We compare a conditional diffusion model (conditioned on flight conditions and target L/D), a gradient-based optimizer on the same surrogate and box constraints, and a *diffusion–optimization hybrid* that first samples diverse candidates with the conditional diffusion model and then locally refines them through the same gradient-based optimizer for near-exact target lift to drag adherence.

Our objective is to facilitate systematic investigation of field-level aerodynamics, to enable rigorous and standardized model comparisons, and to provide a reproducible framework that supports future scaling and multi-condition dataset extensions. An overview of the data pipeline, surrogate families, and inverse-design setup is shown in Fig. 1.

Table 2: Comparison of a few 3D Aircraft Aerodynamic Datasets and Case Studies

Type	Name	Size	Aerodynamic Values			Modalities	BWB	Open Source
			C_L / C_D	C_M	Pointwise C_p / C_f			
Case Study	NASA BWB-450-1L [2]	1 geometry, 27 conditions	✓	✓	✗	Physical	✓	✗
	NASA/Boeing X-48B BWB [1]	2 geometries, 10+ conditions	✓	✓	✗	Physical	✓	✗
	SACCON Dataset [16]	1 geometry, 40K+ conditions	✓	✓	✗	Physical	✓	✗
	NASA CRM [17] (DPW [18] + ETW[19] CFD)	1 geometry	✓	✓	✓	Mesh, Parametric	✗	Partial*
Dataset	AircraftVerse[20]	27,714 geometries	✓	✗	✗	Mesh, Parametric	✗	✓
	ShapeNet Aircraft[21]	4,045 geometries	✓	✗	✗	Mesh, 2D images	✗	✓
	Martín et al. (2025) [22]	1,500 geometries, 1 condition	✓	✓	✗	Parametric	✓	✗
	BlendedNet	1099 geometries, ~10 conditions	✓	✓	✓	Mesh, Parametric	✓	✓
	BlendedNet++	12,490 geometries, 1 condition	✓	✓	✓	Mesh, Parametric	✓	✓

*Select mesh files (‘.bdf’) and structural results (‘.f06’) are available, but full aerodynamic datasets (e.g., full CFD or wind tunnel data) are not openly accessible.

2 Related Work

The Blended Wing Body (BWB) configuration has long been researched for improved fuel burn, lower emissions, and reduced noise pollution. Before modern CFD matured, wind-tunnel programs and flight demonstrators (e.g., X-48) established the aerodynamic and structural promise of BWBs, higher lift-to-drag at lower structural mass [1, 2]. With high-fidelity analysis now routine, BWB conceptual-to-detailed design increasingly couples aerodynamics, structures, and controls through planform parameterizations and MDO [12, 23, 24]. Nevertheless, accurately capturing BWB flow physics early in design remains costly [25], motivating complementary data-driven surrogates that emulate high-fidelity aerodynamics at much lower runtime.

²Dataset available at: <https://doi.org/10.7910/DVN/VJT9EP>

BlendedNet++ Overview – Dataset → Surrogates → Inverse Design

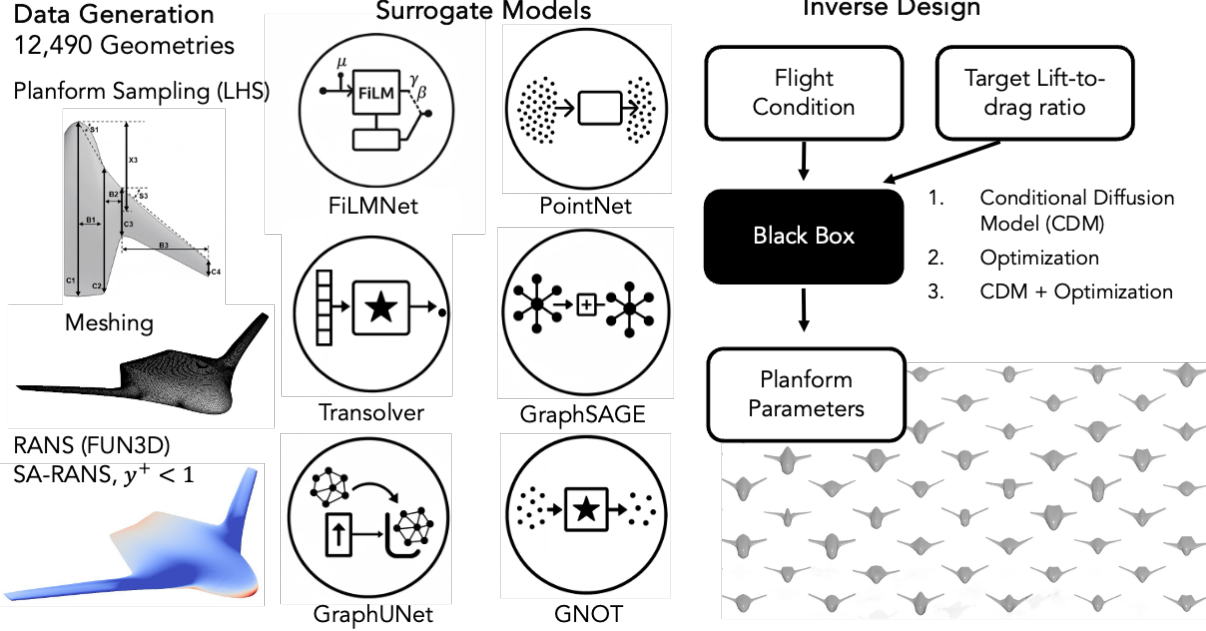


Figure 1: BlendedNet++ overview: (left) geometry parameterization and meshing, (middle) surrogate benchmarks for field-level prediction (FiLMNet, Transolver, PointNet, GraphSAGE, GraphUNet, GNOT), and (right) inverse-design pipeline (conditional diffusion, gradient-based optimization) over the 9-D planform box. The dataset couples integrated coefficients (C_L , C_D , C_M) with dense surface fields C_p and C_f for 12,490 unique BWB geometries.

Design Optimization Methods

Early BWB planform platforms enabled systematic, constraint-aware shape exploration [12, 26]. At the system level, surveys of MDO architectures formalize coupling across disciplines and decomposition strategies [23], while gradient-based high-fidelity shape optimization has delivered measurable BWB gains under realistic constraints [4, 24]. To manage cost, multi-fidelity strategies trade accuracy and speed across tiers of models [13–15], using low/medium-fidelity analyses to scout the space and selectively invoking RANS for refinement. More broadly, emerging *third-generation MDO* frameworks emphasize distributed solver coupling and knowledge sharing across institutions, highlighting the need for standardized workflows and semantic representations to orchestrate large-scale BWB studies [27]. These lines of work remain the gold standard for final design, but still depend on repeated expensive CFD solves, precisely where learned surrogates can accelerate iteration and broaden design-of-experiments.

Public Datasets and Benchmarks

Public aerodynamic resources span focused case studies and broader shape corpora. Case studies include NASA BWB and X-48 programs [1, 2], SACCON [16], and the NASA CRM across DPW/ETW campaigns [17–19]. Broader corpora such as AircraftVerse [20] and ShapeNet-Aircraft [21] emphasize geometry (meshes, parametrics, or 2D images), usually with integrated or proxy aerodynamic targets. Critically for machine learning, dense *surface fields* suitable for field-level learning are rare. **BlendedNet** [11] addressed this gap with 1099 BWB geometries across multiple flight conditions, releasing per-point C_p and C_f and demonstrating low field-level error with learned surrogates. **BlendedNet++** scales this line: 12,490 unique BWBs (one flight condition each), geometry-disjoint splits, and standardized forward/inverse baselines (refer to Table 2), enabling apples-to-apples comparisons across modern surrogate families at significantly larger scale.

Machine Learning for Aerodynamic Prediction

Machine learning (ML) is used to reduce the cost and turnaround time of aerodynamic studies. Purely physics-based CFD can be slow and sensitive to noise and changing flight conditions, especially when exploring large design spaces

[6, 7]. In conventional aircraft settings, researchers have used Gaussian processes and artificial neural networks to model aerodynamic performance [7, 28–30]. Deep models such as CNNs and autoencoders handle higher-dimensional shapes and fields, and graph neural networks (GNNs) fit naturally with mesh-like CFD data [6]. The task of predicting dense surface fields (C_p and C_f) from aircraft geometry and flight conditions remains less explored, largely due to the lack of suitable datasets. Recent large-scale datasets with high-fidelity simulations, such as DrivAerNet++ [8–10], have demonstrated that increasing both dataset size and physical fidelity is critical not only for improving predictive accuracy and generalization, but also for systematically uncovering scaling behaviors in aerodynamic learning tasks.

To address this, recent studies argue for data-driven surrogates that emulate high-fidelity aerodynamics and speed up early-stage design and experiment planning [6, 7, 31, 32]. For *surface-field* prediction (dense C_p and C_f), six model families are commonly used:

- **Point-set models (PointNet):** operate directly on unordered surface point clouds using shared MLPs and permutation-invariant pooling. This avoids remeshing and works with irregular sampling [33].
- **Local graph message passing (GraphSAGE):** aggregates neighbor information on a surface graph to capture short-range aerodynamic effects with good scalability [34].
- **Hierarchical graph encoders (Graph U-Net):** use pooling and unpooling to combine local gradients with global planform trends (e.g., sweep-related shocks), improving multi-scale reasoning [35].
- **Operator-style transformers on graphs (GNOT):** add attention and gating to graph processing so the model can pass information across distant regions of the surface [36].
- **Coordinate transformers (Transolver):** tokenize geometry and physics features and apply physics-aware global attention with near-linear complexity in node count, enabling high-resolution field prediction [37].
- **Hypernetworks (FiLMNet):** inject operating-point context (e.g., flight conditions and planform parameters) via feature-wise scale and shift through the network. This simple conditioning can be applied on top of point, graph, or transformer backbones [38].

These families differ mainly in how they represent geometry (points, graphs, or coordinates) and how they handle long-range interactions (message passing vs. attention).

Inverse Design and Generative Modeling

Classical inverse design. Inverse aerodynamic design has a long history of gradient-based and global optimization approaches built on CFD analyses. Gradient/adjoint methods are effective when smooth design spaces and good initializations are available, and they have been widely adopted within multidisciplinary settings for BWBs (see, e.g., high-fidelity shape optimization within MDO frameworks [4, 23, 24]). When objectives are rugged or multimodal, global strategies such as evolutionary algorithms and Bayesian optimization are commonly used, often in surrogate-assisted loops that alternate between low- and high-fidelity evaluations to manage cost [13–15]. These families emphasize exact constraint handling and CFD-consistent gradients, but they can be sample-intensive when the feasible region is narrow or when designs are strongly coupled to set flight conditions.

Learning-based inverse design. More recently, machine learning has been used to accelerate inverse design. Supervised regressors can map targeted performance to design variables (e.g., mission-level or geometric quantities for BWB-type aircraft [39]), while differentiable surrogates enable gradient-based optimization instead of repeated CFD solves (see also mesh/graph/coordinate surrogates in [6, 38, 40]). Generative models broaden this toolbox by modeling design distributions conditioned on goals or operating points. In 2D airfoil settings, conditional diffusion has been shown to generate shapes that meet coefficient targets [41, 42], and subsequent work extends conditional diffusion to flying-wing concepts across multiple flight conditions [43]. Recently, Martín et al. applied conditional diffusion to the 3D BWB setting, training on a parametric dataset of 1,500 geometries and showing the ability to generate diverse, aerodynamically valid designs directly from target C_L , C_D , and C_M [22]. Compared to direct optimization, generative approaches naturally capture multi-modality in the inverse map (many designs achieving similar targets) and can be combined with downstream refinement or optimization [44]. Across these trends, an emerging pattern is to pair fast learned surrogates (for objectives and constraints) with search or generation mechanisms such as gradient-based, Bayesian/global, or diffusion-based to navigate large, constrained aerodynamic design spaces under realistic flight conditioning.

Limitations of Prior Work

Despite progress, publicly available BWB resources rarely provide *field-resolved* surface data at scale. Most offer only integrated coefficients (C_L , C_D , C_M) or 2D/airfoil cases; when 3D data exist, they usually contain *few geometries*

evaluated across many flight conditions, which complicates geometry dependent generalization. The work that follows targets these gaps.

3 Dataset Generation

The data generation process for this work follows the same process as BlendedNet [11] with some changes made to reduce the number of non-physical geometries generated as well as improvements to the simulation workflow. A blended wing body (BWB) model was parameterically varied to create a set of geometries which are used to create volume meshes for computational fluid dynamics (CFD). The CFD simulations yield integrated force coefficients (1D data) as well as the distribution of pressure and skin friction coefficients across the surface of the aircraft (2D data). Future work may also include the 3D flow fields, but these are excluded here to balance dataset size and ease of use/distribution.

Geometry Generation

The parameterization of the BWB is focused on planform variation. The selected parameters and ranges were inspired by the work of Zhang et al. [12]. The airfoils chosen are fixed and informed by Trac-Pho [45].

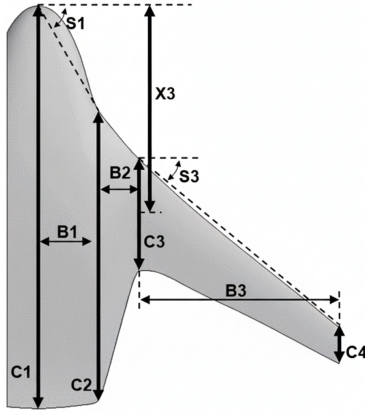


Figure 2: Parameterization of the BWB planform.

Figure 2 illustrates the parameterization of the BWB planform. All length-based parameters are expressed as a ratio of the vehicle centerline length, C_1 . This approach yields 3 chord length fractions, 3 station span fractions, the wing streamwise location fraction, and 2 sweep angles. The summary of these parameters and their ranges can be found in Table 3. Table 4 lists the selected airfoil for each section.

Table 3: Blended wing body planform parameter bounds

Parameter	Min	Max
C_2/C_1	0.55	0.85
C_3/C_1	0.18	0.28
C_4/C_1	0.06	0.09
B_1/C_1	0.10	0.20
B_2/C_1	0.05	0.20
B_3/C_1	0.35	0.70
X_3/C_1	0.50	0.65
$S_1 [^\circ]$	40	60
$S_3 [^\circ]$	20	40

The geometries are defined using the Open Vehicle Sketch Pad (OpenVSP) geometric modeling software [46]. Latin Hypercube Sampling (LHS) was used to select parameters to cover the design space of geometries. For the training dataset 10k geometries were generated. An additional 2.5k independently sampled geometries were created for the test set. All geometries were exported as STEP (.stp) CAD files to feed into the meshing process.

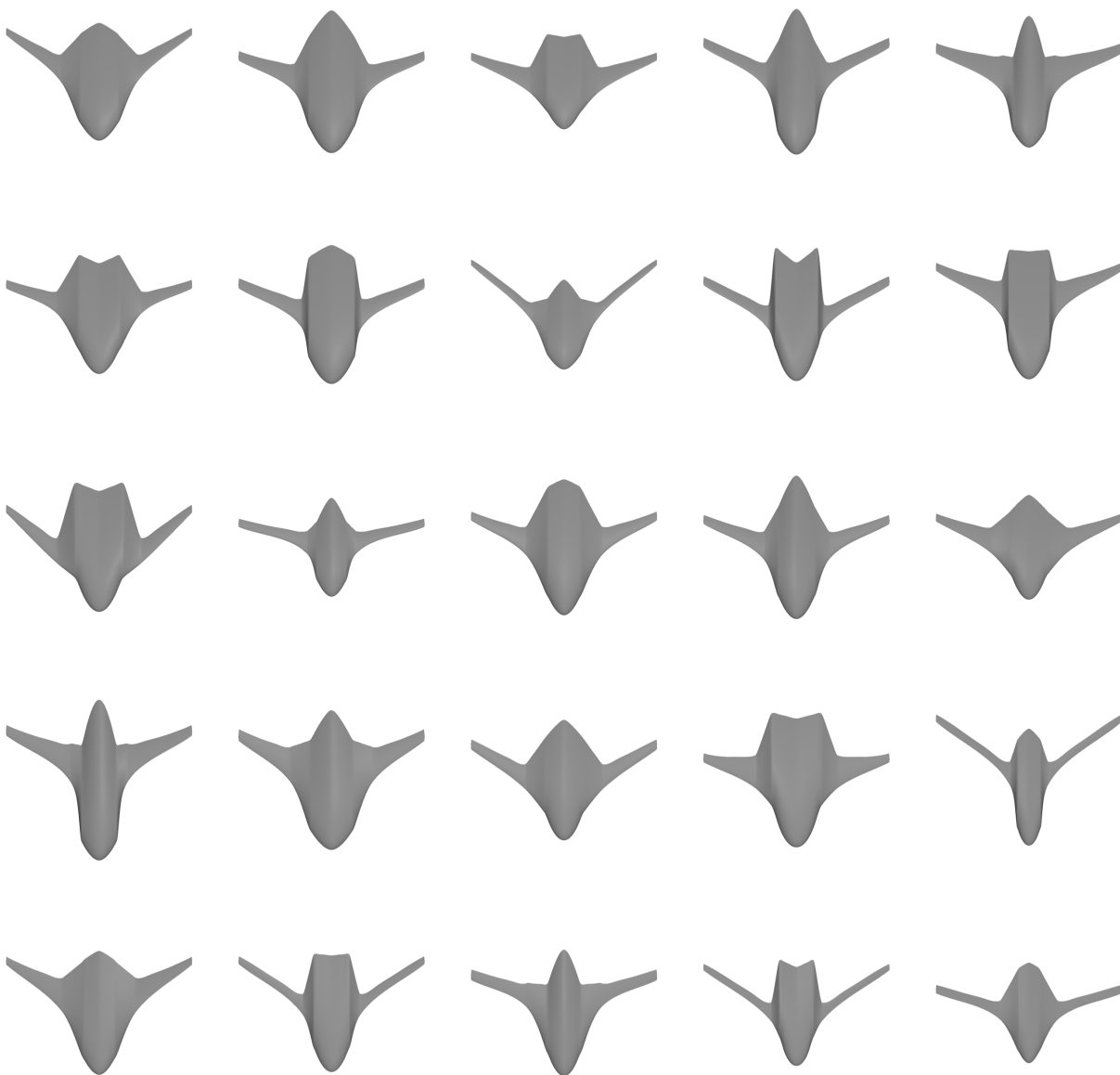


Figure 3: Representative renderings from BlendedNet++, illustrating the shape diversity across the dataset. The variations in fuselage geometry, wing span, and overall configuration highlight the richness of aerodynamic design space captured in the dataset.

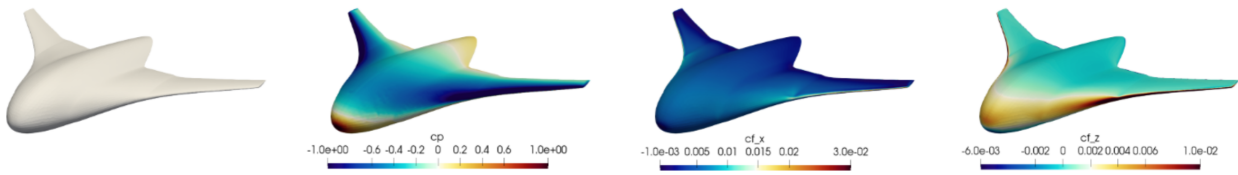


Figure 4: Example from BlendedNet++, showing the 3D shape alongside surface flow quantities. From left to right: baseline geometry, surface pressure coefficient (C_p), and skin-friction coefficients in the streamwise (C_{fx}), and vertical (C_{fz}) directions.

Table 4: Blended wing body airfoil selections

Station	Airfoil
1	NACA 25118
2	NACA 25118
3	NASA SC(2)-0412
4	NACA 0012

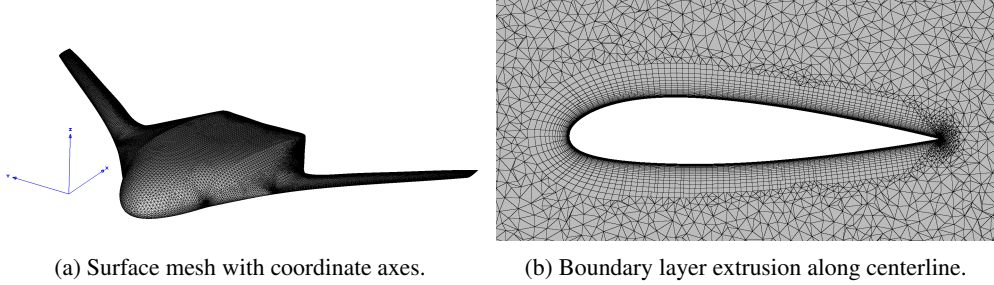


Figure 5: Example visualization of an automatically generated computational fluid dynamics mesh.

Meshing

CFD meshes were generated using the Pointwise meshing software [47]. To facilitate the generation of over 12k meshes, the Pointwise Glyph scripting functionality was leveraged to automate the meshing process. The surface meshes varied between 65k and 162k cells depending on the specific geometry. Volume meshes varied between 6.5 and 11.6 million cells and contain mixed element types. Boundary layer cells were grown off the surface of the aircraft with an initial spacing selected to maintain y^+ values less than 1 in order to accurately resolve the boundary layer. Example visualizations of a mesh can be seen in Figure 5 along with the coordinate axes used. The coordinate system origin is located at the nose of the aircraft.

CFD Simulation

The aerodynamic data was generated using the NASA FUN3D CFD solver [48]. Steady-state simulations were run solving the Reynolds-Averaged Navier-Stokes (RANS) equations using the Spalart-Allmaras turbulence model. A fully resolved, viscous wall boundary condition was applied on the surface of the aircraft and a spherical farfield was applied far from the vehicle for inflow/outflow conditions.

Flight conditions for the CFD cases were sampled using LHS over altitude, Mach number, vehicle centerline length, and angle of attack. The ranges of these parameters as well as their sampling scheme can be seen in Table 5. These sampled parameters allow for the calculation of the simulation inputs: Mach number, Reynolds number, temperature, and angle of attack. Vehicle length was sampled on a log scale in order to smooth the distribution of computed Reynolds number. Reynolds number was not sampled directly as this approach would lead to too much variation in the effective vehicle centerline length, presenting substantial challenges in automating the mesh generation process, specifically for boundary layer resolution. All simulations were completed for a model centerline length of 1 m to simplify the case setup, but the results can be used to predict for the full range of vehicle lengths leveraging the principle of flow similarity (see [49] for detailed discussion). Reference area and reference length for force and moment non-dimensionalization were likewise set to 1 m^2 and 1 m, respectively, to simplify computations. The moment reference location is set to the nose of the vehicle, again for simplicity given the large variation of geometries present in the dataset.

Table 5: Sampling of flight condition inputs

Parameter	Sampling	Range
Altitude [kft]	Linear	[0,40]
Mach [-]	Linear	[0.05,0.5]
Centerline Length [m]	Log	[0.1,10]
Angle of Attack [$^\circ$]	Linear	[-8,16]

Results Processing

A post-processing routine was used to filter non-converged CFD simulations, collect the results of all the converged cases, and create a VTK file for the distributed surface quantities for each case. A residual filter of 1×10^{-8} for density and 1×10^{-6} for turbulence was applied, leading to the training and test sets containing 9992 and 2498 cases, respectively. All converged results were aggregated together to compile the geometry parameters, flight conditions, and integrated lift, drag, and moment coefficients for each run. These scalar outputs for each case are paired with a VTK file [50] containing the surface mesh with the distribution of pressure coefficient (C_p) as well as components of skin friction (C_{fx} , C_{fy} , C_{fz}) across the surface of the aircraft.

4 Dataset Characteristics

The dataset generation process was executed utilizing resources from the MIT Lincoln Laboratory Supercomputing Center [51]. The breakdown of computational time per task can be found in Table 6 along with the compute resource utilized for that task. Figure 3 illustrates representative geometries from BlendedNet++, showcasing the diversity of fuselage shapes, wing spans, and overall configurations present in the dataset. The total dataset is roughly 60 GB (uncompressed) where each VTK file is roughly 5 MB. An example from BlendedNet++ is shown in Figure 4, including the baseline 3D geometry and the corresponding surface flow fields (C_p , C_{fx} , and C_{fz}). To summarize global aerodynamic trends across the dataset, Fig. 6 visualizes key pairwise relationships.

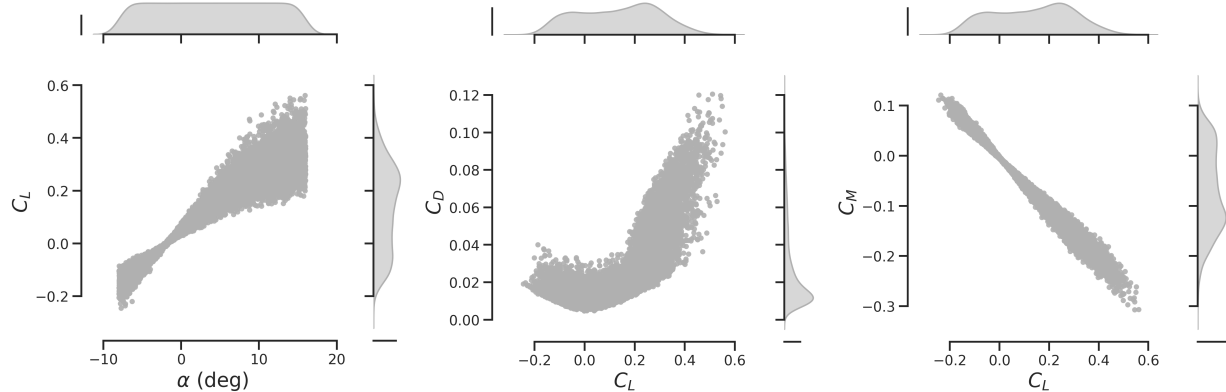


Figure 6: Scatter plots of aerodynamic relationships: (Left) Lift coefficient (C_L) vs angle of attack (α), (Center) Drag coefficient (C_D) vs Lift coefficient (C_L), and (Right) Pitching moment coefficient (C_M) vs Lift coefficient (C_L). These relationships provide insights into aerodynamic performance and longitudinal stability characteristics.

Table 6: Computational cost breakdown for the dataset generation process

Task	Resource	Time per Case
Geometry Generation	Xeon-p8 CPU	10–15 sec
Mesh Generation	Xeon-p8 CPU	3–4 min
CFD Solve	2xV100 GPU	1.5 hr
	2xH100 GPU	30–35 min

The dataset contains a predefined train/test split of 9992 training cases and 2498 testing cases, representing an 80/20 split. As previously stated, the geometry parameters and flight conditions were independently sampled via LHS for each piece of the split.

Comparison to BlendedNet

The BlendedNet++ dataset introduced in this work is an improvement on the previously released BlendedNet dataset [11]. Several enhancements to the dataset generation process distinguish this data from the previous work. The automated meshing routine was improved leading to better quality meshes and improved convergence of the CFD simulations. The previously defined S_2 parameter has been replaced by the X_3 parameter to attempt to minimize

the number of infeasible geometries generated, specifically those where the outboard section of the wing is too far forward on the main body. The simulated angle of attack range was narrowed from $[-10, 20]^\circ$ to $[-8, 16]^\circ$ to increase the density of sampling for more realistic aircraft flight conditions. While BlendedNet++ contains only roughly 2.5k more CFD cases than BlendedNet, each CFD case is for a unique geometry, increasing the diversity of the geometry parameter space. Table 7 highlights some of these changes and contains the specific geometry and CFD case counts between the datasets.

Table 7: Comparison between BlendedNet and BlendedNet++ datasets

Quantity	BlendedNet	BlendedNet++
Total Geometries	1,099	12,490
Training CFD Cases	8830	9992
Testing CFD Cases	870	2498

5 Surrogate Model Development

Why a six-model benchmark? It is often unclear which representation works best for *field-level* surface prediction in aerodynamics, and reported “best model” vary by dataset, resolution, and metric [6–10]. Recent benchmark efforts and editorials argue that progress requires common datasets, geometry-disjoint splits, and unified metrics to separate modeling choices from data curation [52, 53]. We therefore evaluate six complementary families that cover distinct inductive biases while keeping preprocessing minimal and comparable: point-set, local graph message passing, hierarchical graph encoders, operator-style transformers on graphs, coordinate transformers, and FiLM-style hypernetwork conditioning. To isolate architectural effects, we hold inputs, losses, training budget, and evaluation protocols fixed, and implement a shared training loop via the *NeuralSolver* codebase [54]. All six forward surrogates are trained on a single NVIDIA A100 GPU with a shared early-stopping schedule and a maximum wall-clock budget of roughly 24 hours per model.

We benchmark these six forward models for *pointwise* prediction of C_p and C_f : *PointNet*, *Transolver*, *GraphSAGE*, *GraphUNet*, *GNOT*, and *FiLMNet*. Except for FiLMNet, all models are implemented and trained using *NeuralSolver* [54]. FiLMNet follows the BlendedNet architecture [11]. We omit the spanwise skin-friction C_{f_y} because the zero-sideslip, symmetric BWB setup implies near-zero integrated side force, making C_{f_y} negligible for C_L and C_D relative to C_p , C_{f_x} , and C_{f_z} . The dataset still includes C_{f_y} for completeness. Full architectural choices, hyperparameters, and training details are provided in the Appendix. Code and scripts will be released to ensure reproducibility. We do not claim these configurations are globally optimal. They are controlled, representative baselines chosen to compare inductive biases.

5.1 Feature-wise Linear Modulation (FiLMNet)

The FiLMNet predicts

$$u_i = [C_p(x_i, n_i), C_{f_x}(x_i, n_i), C_{f_z}(x_i, n_i)] \in \mathbb{R}^3$$

at each surface point i from a base MLP that takes *only* the pointwise geometry

$$s_i = [x_i, n_i] \in \mathbb{R}^6,$$

while the layer-wise modulation is conditioned on the 12 broadcast variables

$$\mu = [\log_{10} Re_L, M_\infty, \alpha, B1, B2, B3, C2, C3, C4, S1, S3, X3] \in \mathbb{R}^{12}.$$

Let $h_0 = s_i$ and h_ℓ be the hidden activation at layer ℓ of the base MLP. A small hypernetwork h_ψ maps μ to FiLM parameters $(\gamma_\ell, \beta_\ell)$ per layer, and we apply FiLM as

$$\tilde{h}_\ell = \gamma_\ell(\mu) \odot h_\ell + \beta_\ell(\mu), \quad h_{\ell+1} = \sigma(W_\ell \tilde{h}_\ell + b_\ell),$$

with \odot denoting elementwise multiplication and σ a pointwise nonlinearity. The output head maps the final activation to $u_i \in \mathbb{R}^3$.

5.2 PointNet

PointNet [33] is a deep-learning architecture that directly processes 3D point clouds by applying shared multilayer perceptrons (MLPs) to each point and then aggregating features via a permutation-invariant operator (e.g., max pooling).

$$\mathbf{fx} = \left[\underbrace{\log_{10} Re_L, M_\infty, \alpha}_{3 \text{ flight conditions}}, \underbrace{B_1/C_1, B_2/C_1, B_3/C_1, C_2/C_1, C_3/C_1, C_4/C_1, S_1, S_3, X_3/C_1}_{9 \text{ geometric parameters}}, \underbrace{n_x, n_y, n_z}_{\text{surface normals}} \right]. \quad (1)$$

Our adaptation. Each point supplies its 3D coordinates (x, y, z) and a 15-D feature vector: the 9 planform parameters and 3 flight conditions (broadcast to all points) plus the 3 local surface normals (n_x, n_y, n_z) . We concatenate coordinates and features at the input and regress (C_p, C_f) .

5.3 Transolver

Transolver introduces Physics-Attention to improve neural operators on irregular meshes by aggregating points into physics-aware tokens and attending over tokens. It has been reported to perform competitively on irregular-mesh PDE surrogate tasks and flow problems, with strong accuracy for long-range interactions and near-linear scaling in the number of surface points due to efficient attention approximations [37]. It captures nonlocal coupling via attention, works directly on point clouds without remeshing or UV parameterization, scales to high-resolution surfaces through tokenization, and ships with a maintained open-source implementation that supports reproducibility [37]. We treat Transolver as representative of coordinate and point-token transformer-based models for field prediction.

Our adaptation. The current Transolver implementation targets fixed PDE setups and does not adjust for varying boundary conditions or changing geometries as inputs. Our prediction task varies *both*, so we condition the model explicitly by concatenating the flight conditions and planform geometries as additional features to every surface node. We use the same input preparation as in Eq. (1): coordinates $x \in \mathbb{R}^{N \times 3}$ and per-point features $\mathbf{fx} \in \mathbb{R}^{N \times 15}$ (9 planform parameters and 3 flight conditions plus the 3 local surface normals (n_x, n_y, n_z)), concatenated at the input. The concatenated node features are then processed by Physics-Attention so flight conditions and geometric features inform the slice tokens.

5.4 GraphSAGE

GraphSAGE [6] adapts neighborhood aggregation to aerodynamic prediction by building dynamic k -NN graphs from 3D surface meshes and flight conditions. Each node encodes spatial coordinates (x, y, z) , surface normals (n_x, n_y, n_z) , and flight conditions (Reynolds number Re_L , Mach number M_∞ , and angle of attack α).

Our adaptation. We sample 1024 surface points per geometry, construct graphs with $k = 15$ neighbors, and concatenate condition features at every node. Three GraphSAGE layers with 128 hidden dimensions apply mean aggregation with residual connections, followed by layer normalization and dropout ($p = 0.2$). Mixed-precision training and GPU-accelerated k-NN search ensure efficiency during large-scale experiments.

5.5 GraphUNet

GraphUNet [35] extends the U-Net architecture to graphs by hierarchically downsampling and upsampling node embeddings through graph pooling and unpooling layers. This structure allows the network to capture both local and global dependencies while preserving resolution for pointwise predictions.

Our adaptation. We construct dynamic k -NN graphs ($k = 20$) from surface points augmented with normals and operating conditions, using subsampled point clouds of 1024 points per geometry. The input features combine spatial coordinates, surface normals, and flight conditions. We employ five U-Net levels with SAGE convolution layers of 128 hidden dimensions, random pooling with ratio 0.5, and skip connections for feature reuse. Layer normalization and dropout ($p = 0.2$) provide regularization, and mixed-precision training is used for efficiency on large-scale datasets.

Compared to other point-cloud-based models, the graph-based architectures actually showed degraded performance when geometric parameters were included, so we excluded them from the final training setup based on empirical results.

5.6 GNOT (Graph Neural Operator Transformer)

GNOT [36] is a operator-learning transformer over graphs with global attention to model long-range interactions.

Our adaptation. We follow the same input preparation as in Eq. (1), providing coordinates $x \in \mathbb{R}^{N \times 3}$ and the per-point feature vector $\mathbf{fx} \in \mathbb{R}^{N \times 15}$, concatenated at the input. GNOT takes (x, \mathbf{fx}) as input to predict (C_p, C_f) , using global attention to capture nonlocal aerodynamic coupling.

5.7 Training Objective

We predict three per-point channels: (i) pressure coefficient C_p , (ii) skin-friction in the streamwise direction C_{f_x} , and (iii) skin-friction in the vertical direction C_{f_z} . We train on their normalized forms $\tilde{C} = (C - \mu)/\sigma$. For N surface points, the loss is

$$\mathcal{L} = \frac{1}{N} \sum_{i=1}^N \left[(\hat{\tilde{C}}_{p,i} - \tilde{C}_{p,i})^2 + (\hat{\tilde{C}}_{f_x,i} - \tilde{C}_{f_x,i})^2 + (\hat{\tilde{C}}_{f_z,i} - \tilde{C}_{f_z,i})^2 \right], \quad (2)$$

where hats denote predictions and tildes denote normalized targets.

6 Inverse Design via Conditional Diffusion

We pose inverse design as conditional generation $p(p | \mu)$ where $p \in \mathbb{R}^9$ lies in a box \mathcal{B} (Table 3), and

$$\mu = [\text{alt}_{\text{kft}}, \log_{10}(\text{Re}_L), M_\infty, \alpha_{\text{deg}}, (L/D)_{\text{target}}] \in \mathbb{R}^5.$$

A denoising diffusion model parameterizes p_θ , and samples are projected onto \mathcal{B} . Full architectural choices, hyperparameters, and training details are provided in the Appendix.

6.1 Model

We employ a residual MLP denoiser f_θ that predicts additive noise $\hat{\epsilon}$ given a noised geometry vector x_t , diffusion timestep t , and condition μ :

$$\hat{\epsilon} = f_\theta(x_t, t, \mu).$$

The timestep t and μ are embedded by separate linear projections and concatenated with x_t ; a stack of residual MLP blocks maps to a linear head in \mathbb{R}^9 (represents the 9 geometric parameters). A cosine β_t schedule defines $\alpha_t = 1 - \beta_t$ and the cumulative product $\bar{\alpha}_t = \prod_{s=1}^t \alpha_s$.

6.2 Forward (Noising) Process

The training target x_0 is the normalized geometry vector. We draw noise $\epsilon \sim \mathcal{N}(0, I)$ and sample

$$q(x_t | x_0) = \mathcal{N}(\sqrt{\bar{\alpha}_t} x_0, (1 - \bar{\alpha}_t)I), \quad x_t = \sqrt{\bar{\alpha}_t} x_0 + \sqrt{1 - \bar{\alpha}_t} \epsilon.$$

6.3 Training Objective

We optimize the standard noise-prediction loss

$$\mathcal{L}(\theta) = \mathbb{E}_{x_0, \mu, t, \epsilon} \left[\|\epsilon - f_\theta(x_t, t, \mu)\|_2^2 \right],$$

which is equivalent (up to constants) to a variational bound when the model predicts ϵ . Cosine β_t , sinusoidal t -embeddings, and residual MLP blocks follow common practice for conditional DDPMs.

6.4 Conditioning and Normalization

We standardize μ (with $\log_{10}(\text{Re}_L)$ as an input) using a fitted $\mathcal{N}(0, 1)$ scaler. Geometry parameters are scaled to $[-1, 1]$ during training and denormalized only at sampling.

6.5 Sampling

Given a condition μ , we first standardize it, then draw $x_T \sim \mathcal{N}(0, I)$ and iterate for $t = T, \dots, 1$:

$$\hat{x}_0 = \frac{1}{\sqrt{\bar{\alpha}_t}} \left(x_t - \sqrt{1 - \bar{\alpha}_t} \hat{\epsilon}_\theta(x_t, t, \mu) \right).$$

The reverse mean and variance are

$$\begin{aligned} \mu_\theta(x_t, t, \mu) &= \frac{\beta_t \sqrt{\bar{\alpha}_{t-1}}}{1 - \bar{\alpha}_t} \hat{x}_0 + \frac{(1 - \bar{\alpha}_{t-1}) \sqrt{\alpha_t}}{1 - \bar{\alpha}_t} x_t, \\ \sigma_t^2 &= \frac{\beta_t (1 - \bar{\alpha}_{t-1})}{1 - \bar{\alpha}_t}. \end{aligned} \quad (3)$$

We then sample

$$x_{t-1} = \begin{cases} \mu_\theta(x_t, t, \mu) + \sigma_t z, & t > 1, z \sim \mathcal{N}(0, I), \\ \mu_\theta(x_t, t, \mu), & t = 1. \end{cases}$$

Finally, we invert the geometry scaler to obtain physical units $p = \text{denorm}(x_0)$. For each μ , we draw $K = 100$ i.i.d. samples to quantify diversity and performance (Section 7.2).

7 Results and Discussion

7.1 Forward Benchmark Results

Table 8: Forward prediction errors on the *unseen test* set. Pointwise field metrics.

Model	Params	C_p				C_{fx}				C_{fz}			
		MSE ($\times 10^{-2}$)	MAE ($\times 10^{-2}$)	RelL1 (%)	RelL2	MSE ($\times 10^{-6}$)	MAE ($\times 10^{-3}$)	RelL1 (%)	RelL2	MSE ($\times 10^{-6}$)	MAE ($\times 10^{-4}$)	RelL1 (%)	RelL2
GNOT	11,496,219	9.66	17.04	61.45	39.79	22.94	2.155	57.96	38.47	13.91	12.41	65.91	41.68
GraphUNet	13,978,499	2.35	8.96	29.45	28.08	16.00	1.53	32.68	47.48	6.00	10.51	53.28	38.71
GraphSAGE	407,811	1.06	5.65	18.59	18.86	11.00	1.17	25.03	39.86	4.00	7.66	38.80	31.38
PointNet	919,107	0.974	6.541	23.59	4.01	7.95	1.683	45.28	13.32	1.94	4.94	26.24	5.81
Transolver	2,816,067	0.901	6.075	21.91	3.71	7.03	1.437	38.67	11.79	1.48	3.57	18.97	4.44
FiLMNet	795,651	0.418	2.147	7.11	1.42	6.50	0.682	14.64	9.15	1.65	3.81	19.38	4.54

Table 8 reports pointwise errors (MSE, MAE, RelL1, RelL2). The results indicate that the most pronounced differences between models occur in the C_p relative errors, where FiLMNet delivers the best performance, demonstrating the effectiveness of lightweight feature-wise conditioning for surface pressure prediction. Transolver follows, with reasonable accuracy that we hypothesize benefits from physics-aware attention, though it does not reach FiLMNet’s level. PointNet performs noticeably better than graph-based approaches, capturing pressure trends more accurately despite its simple point-set design. In contrast, GraphSAGE and GraphUNet both lag behind: GraphSAGE struggles with higher pressure errors despite having fewer parameters, while GraphUNet’s added hierarchical complexity does not translate into improved accuracy. GNOT performs the worst overall, suggesting that heavy operator-style transformers are less suited for this dataset without additional inductive bias or larger-scale training. Overall, FiLMNet stands out as the most accurate and efficient surrogate, with PointNet and Transolver as a strong baseline.

7.2 Inverse Design

Inverse design is posed as conditional generation of planform parameters $p \in \mathbb{R}^9$ (Table 3) given a flight condition μ and a target lift-to-drag ratio (L/D). For each of the 2,498 test conditions, we generate 100 samples with a conditional diffusion model (CDM). As a baseline, we run multi-start gradient-based optimization (“Opt”) on the same evaluation surrogate, with 100 random initial seeds per condition and projected updates to respect bounds. A hybrid (“CDM→Opt”) refines each CDM sample via a short local optimization pass.

We report two aspects per condition, then average across all conditions: (i) *accuracy* w.r.t. the L/D target using R^2 (higher is better), RMSE (lower), and MAE (lower); and (ii) *diversity* of generated parameters using mean pairwise distance (MPD; larger spread is better) and mean nearest-neighbor distance (MinDist; larger indicates more even spacing) computed in standardized parameter space.

Table 9: Inverse design results averaged over 2,498 conditions. Accuracy (left; *computed w.r.t. the surrogate-predicted L/D*) and diversity (middle). Runtime (right) reports wall-clock per condition to produce 100 samples. Values are mean \pm std across conditions; R^2 is computed globally across all rows. Better: $R^2 \uparrow$, RMSE/MAE \downarrow , MPD/MinDist \uparrow .

Method	Accuracy to target L/D			Diversity in parameter space		Runtime (100 samples)
	$R^2 \uparrow$	RMSE \downarrow	MAE \downarrow	MPD (spread) \uparrow	MinDist (uniformity) \uparrow	
CDM	0.99609	0.338 ± 0.257	0.319 ± 0.260	1.802 ± 0.523	0.621 ± 0.106	~ 0.3 s
Opt	0.99187	0.559 ± 0.251	0.481 ± 0.250	3.867 ± 0.106	1.806 ± 0.072	~ 3 s
CDM→Opt	0.99995	0.017 ± 0.045	0.016 ± 0.044	1.725 ± 0.505	0.569 ± 0.107	~ 0.9 s

Runtime notes: Opt uses 1000 Projected Gradient Descent (PGD) steps; CDM is forward sampling only; CDM→Opt is CDM sampling + 200 PGD steps.

Initialization: Opt starts from 100 random seeds uniformly sampled within the planform box \mathcal{B} defined by the bounds in Table 3; CDM draws 100 samples using independent Gaussian noise seeds per condition. Runtimes measured on a single NVIDIA RTX 4090 GPU.

Initialization: Opt starts from 100 random seeds uniformly sampled within the planform box \mathcal{B} defined by the bounds in Table 3; CDM draws 100 samples using independent Gaussian noise seeds per condition.

CDM better matches prescribed L/D targets than Opt (higher R^2 , lower RMSE/MAE), but explores a *smaller* region of design space. In contrast, Opt is more exploratory and uniform (highest MPD and MinDist), though its target-tracking accuracy is weaker. *In terms of speed, CDM sampling is $\sim 10\times$ faster than Opt per condition (about 0.3 s vs. 3 s for 100 samples), as shown in Table 9.* The hybrid CDM→Opt achieves near-perfect accuracy, but further reduces diversity (lower MPD and MinDist than both CDM and Opt) as many seeds converge to nearby optima. To relate these *refined* designs to the data manifold, we additionally validate the resulting *geometries* against ground-truth geometries.

Over the 2,498 test conditions, we compare each condition’s true planform to the set of generated samples (100 per condition). We use a scale-invariant *mean relative error* over the 9 planform parameters

$$\text{mRE}(g, t) = \frac{1}{9} \sum_{j=1}^9 \frac{|g_j - t_j|}{\text{range}_j}, \quad \text{range}_j = \max_{\text{test}} p_j - \min_{\text{test}} p_j.$$

Two key findings at a 20% mRE threshold:

- **18.39%** of samples per condition match the test geometry (i.e., $\text{mRE} \leq 0.20$).
- **60.89%** of conditions have *at least one* generated sample within $\text{mRE} \leq 0.20$.

These results validate the **CDM→Opt** procedure as effective for producing geometries close to the *true* test designs under the reported tolerance. Importantly, it also shows that the inverse problem is underdetermined, that is, many distinct planforms can satisfy the same $(\mu, L/D)$ target.

CFD validation of inverse designs

To verify that surrogate-based inverse designs remain valid under high-fidelity flow solving, we re-simulated one *CDM→Opt* sample per test condition with FUN3D and compared the CFD-evaluated L/D against the surrogate’s L/D for those designs. Across all conditions, correlation is excellent ($R^2 = 0.9974$), supporting the functionality of the diffusion–optimization pipeline.

8 Conclusion, Limitations, and Future Work

We have presented **BlendedNet++**, a large-scale blended wing body (BWB) aerodynamic dataset comprising 12,490 unique geometries, each with dense surface pressure and skin-friction fields. Alongside the dataset, we introduced standardized, geometry-disjoint splits and a forward-surrogate benchmark spanning six model families: *PointNet*, *GraphSAGE*, *GraphUNet*, a coordinate transformer (*Transolver*), *FilmNet*, and the *Graph Neural Operator Transformer* (GNOT). We also developed inverse-design baselines that include conditional diffusion, gradient-based optimization, and a diffusion–optimization hybrid, providing reproducible methods for generating and refining candidate designs.

Limitations and design choices. (1) *Single condition per geometry.* We deliberately use one flight condition per geometry to maximize *geometric diversity* and keep supervision scalable. In our experience, field-level surrogates gain more from breadth of shapes than from per-geometry flight condition sweeps. Moreover, the 12,490 unique-geometry corpus—with LHS-sampled flight variables—still provides broad coverage of the operating envelope. (2) *Surface fields only.* We focus on C_p and C_f over the surface to keep storage and I/O manageable and to target the quantities most directly used for forces and moments. This precludes

²Runtimes measured on a single NVIDIA RTX 4090 GPU.

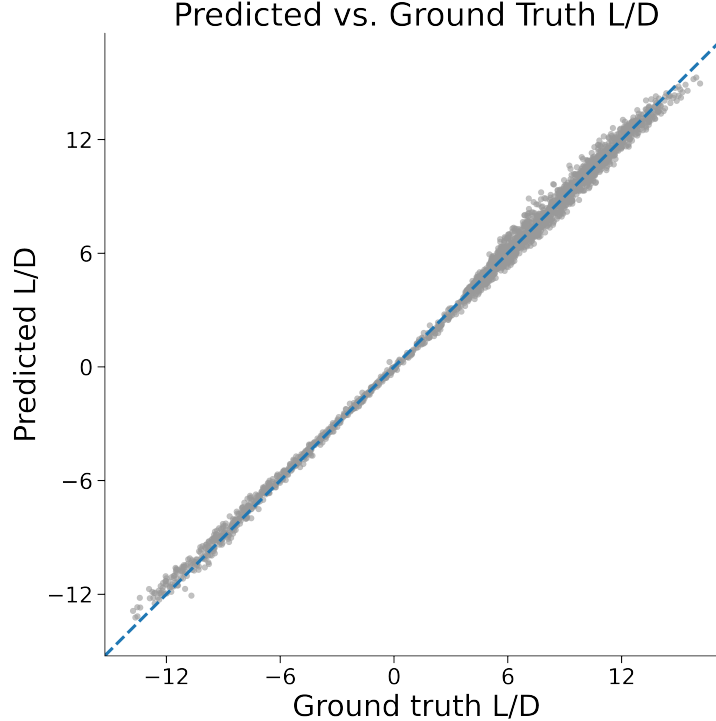


Figure 7: CFD-validated inverse designs: FUN3D L/D versus surrogate-predicted L/D for one $CDM \rightarrow Opt$ sample per condition. Overall correlation is $R^2 = 0.9974$.

operator-learning studies on full volumetric flow fields in the current release. (3) *CFD and meshing fidelity*. Automated meshing at scale can introduce variability in near-wall resolution and element quality, and steady RANS with a single turbulence model may deviate from true flow physics for separated or highly three-dimensional regimes. These choices reflect a balance between throughput and fidelity for a first large release.

Future directions. We see several extensions as especially impactful: (i) matched *multi-condition* cohorts per geometry (and potentially unsteady/transient cases) to probe condition coupling (ii) inclusion of *volumetric* fields to enable operator-learning beyond the surface (iii) curated *higher-fidelity* and/or experimental subsets (e.g., DES/LES or wind-tunnel comparisons) for cross-validation (iv) richer, *constrained* inverse-design tasks that couple aerodynamics with structural/mission constraints and uncertainty quantification and (v) community-facing *leaderboards/challenge tracks* on the provided splits to encourage fair, reproducible progress.

Overall, BlendedNet++ is intended as a foundation rather than a finished endpoint: the benchmark configurations are representative baselines (not claimed optimal), and the dataset and code are structured to support systematic scaling, ablations, and community-driven extensions.

Acknowledgments

The authors acknowledge the MIT Lincoln Laboratory Supercomputing Center for providing HPC resources that contributed to these results [51].

© 2025 Massachusetts Institute of Technology.

Delivered to the U.S. Government with Unlimited Rights, as defined in DFARS Part 252.227-7013 or 7014 (Feb 2014). Notwithstanding any copyright notice, U.S. Government rights in this work are defined by DFARS 252.227-7013 or DFARS 252.227-7014 as detailed above. Use of this work other than as specifically authorized by the U.S. Government may violate any copyrights that exist in this work.

References

- [1] R. H. Liebeck. Design of the blended wing body subsonic transport. *Journal of Aircraft*, 41(1):10–25, 2004. doi: 10.2514/1.9244.

- [2] Melissa Carter, Dan Vicroy, and Dharmendra Patel. Blended-wing-body transonic aerodynamics: Summary of ground tests and sample results. In *47th AIAA Aerospace Sciences Meeting including the New Horizons Forum and Aerospace Exposition*, Orlando, FL, Jan 2009. doi: 10.2514/6.2009-935. AIAA Paper 2009-935.
- [3] Zhenli Chen, Minghui Zhang, Yingchun Chen, Weimin Sang, Zhaoguang Tan, Dong Li, and Binqian Zhang. Assessment on critical technologies for conceptual design of blended-wing-body civil aircraft. *Chinese Journal of Aeronautics*, 32(8): 1797–1827, Aug 2019. doi: 10.1016/j.cja.2019.03.008.
- [4] Achyuth Attravanam. *High-fidelity CFD-based Shape Optimization of a Blended-Wing-Body Aircraft for Improved Aerodynamic Performance, Considering Engine Integration Effects*. Phd dissertation, Technische Universität Braunschweig, 2023.
- [5] Shang Lyu, Yicheng Sun, Joseph L. Chan, and Howard Smith. Blended wing body aircraft conceptual design optimisation with nonlinear multi-fidelity aerodynamic surrogate model. In *AIAA Aviation Forum and ASCEND*, 2024. doi: 10.2514/6.2024-3979. AIAA Paper 2024-3979.
- [6] Yiqun Dong, Jun Tao, Youmin Zhang, Wei Lin, and Jianliang Ai. Deep learning in aircraft design, dynamics, and control: Review and prospects. *IEEE Transactions on Aerospace and Electronic Systems*, 57(4):2346–2368, 2021. doi: 10.1109/TAES.2021.3056082.
- [7] Christian Sabater, Philipp Stürmer, and Philipp Bekemeyer. Fast predictions of aircraft aerodynamics using deep-learning techniques. *AIAA Journal*, 60(9):5249–5261, September 2022. doi: 10.2514/1.J061145.
- [8] Mohamed Elrefaie, Florin Morar, Angela Dai, and Faez Ahmed. Drivaernet++: A large-scale multimodal car dataset with computational fluid dynamics simulations and deep learning benchmarks. *Advances in Neural Information Processing Systems*, 37:499–536, 2024.
- [9] Mohamed Elrefaie, Angela Dai, and Faez Ahmed. Drivaernet: A parametric car dataset for data-driven aerodynamic design and prediction. *Journal of Mechanical Design*, 147(4):041712, 2025.
- [10] Mohamed Elrefaie, Angela Dai, and Faez Ahmed. Drivaernet: A parametric car dataset for data-driven aerodynamic design and graph-based drag prediction. In *International Design Engineering Technical Conferences and Computers and Information in Engineering Conference*, volume 88360, page V03AT03A019. American Society of Mechanical Engineers, 2024.
- [11] Nicholas Sung, Steven Spreizer, Mohamed Elrefaie, Kaira Samuel, Matthew C. Jones, and Faez Ahmed. Blendednet: A blended wing body aircraft dataset and surrogate model for aerodynamic predictions. In *Proceedings of the ASME 2025 International Design Engineering Technical Conferences and Computers and Information in Engineering Conference (IDETC/CIE 2025)*, Anaheim, CA, USA, August 2025. ASME.
- [12] M. H. Zhang, Z. L. Chen, and B. Q. Zhang. A conceptual design platform for blended wing-body transports. In *Proceedings of the 30th Congress of the International Council of the Aeronautical Sciences (ICAS)*, pages 25–30, Daejeon, South Korea, Sep 2016.
- [13] Alex Feldstein, David Lazzara, Norman Princen, and Karen Willcox. Multifidelity data fusion: Application to blended-wing-body multidisciplinary analysis under uncertainty. *AIAA Journal*, 58(2):889–906, 2020.
- [14] Soumalya Sarkar, Sudepta Mondal, Michael Joly, Matthew E. Lynch, Shaunak D. Bopardikar, Ranadip Acharya, and Paris Perdikaris. Multifidelity and multiscale bayesian framework for high-dimensional engineering design and calibration. volume 141, page 121001, Dec 2019. doi: 10.1115/1.4044543.
- [15] Nikoleta Dimitra Charisi, Hans Hopman, and Austin A Kana. Multi-fidelity design framework integrating compositional kernels to facilitate early-stage design exploration of complex systems. *Journal of Mechanical Design*, 147(1):011701, 2025.
- [16] Thomas D. Loeser and Andreas Schuette. Saccon forced oscillation tests at dnw-nwb and nasa langley 14x22-foot tunnel. In *28th AIAA Applied Aerodynamics Conference*, Chicago, IL, Jun 2010. doi: 10.2514/6.2010-4394. AIAA Paper 2010-4394.
- [17] Melissa B. Rivers. Nasa common research model: A history and future plans. In *AIAA Aviation 2019 Forum*, Dallas, TX, Jun 2019. doi: 10.2514/6.2019-3725. AIAA Paper 2019-3725.
- [18] Anthony Sclafani, John Vassberg, Mortaza Mani, Chad Winkler, Andrew Dorgan, Michael Olsen, and James Coder. Dpw-5 analysis of the crm in a wing-body configuration using structured and unstructured meshes. In *51st AIAA Aerospace Sciences Meeting Including the New Horizons Forum and Aerospace Exposition*, Grapevine, TX, Jan 2013. doi: 10.2514/6.2013-0048. AIAA Paper 2013-0048.
- [19] Thorsten Lutz. Going for experimental and numerical unsteady wake analyses combined with wall interference assessment by using the nasa crm-model in etw. In *51st AIAA Aerospace Sciences Meeting Including the New Horizons Forum and Aerospace Exposition*, Grapevine, TX, Jan 2013. doi: 10.2514/6.2013-0871. AIAA Paper 2013-0871.
- [20] Adam Cobb, Anirban Roy, Daniel Elenius, Frederick Heim, Brian Swenson, Sydney Whittington, James Walker, Theodore Bapty, Joseph Hite, Karthik Ramani, and Craig McComb. Aircraftverse: A large-scale multimodal dataset of aerial vehicle designs. *Advances in Neural Information Processing Systems*, 36:44524–44543, Dec 2023.
- [21] Kristen M. Edwards, Vaishnavi L. Addala, and Faez Ahmed. Design form and function prediction from a single image. In *Proceedings of the ASME 2021 International Design Engineering Technical Conferences and Computers and Information in Engineering Conference (IDETC-CIE)*, volume 85376, page V002T02A032, Virtual Conference, Aug 2021. American Society of Mechanical Engineers. doi: 10.1115/DETC2021-68566.

- [22] Marta A. Martín, Andrés Mateo-Gabín, Thomas Wagenaar, Gonzalo Rubio, and Sven A. Lanzan Ferran. Ai-based generative algorithms applied to the design of blended wing body aircraft. In *AIAA Aviation Forum and ASCEND 2025*, Las Vegas, NV, United States, July 2025. doi: 10.2514/6.2025-3292.
- [23] Joaquim R. R. A. Martins and Andrew B. Lambe. Multidisciplinary design optimization: A survey of architectures. *AIAA Journal*, 51(9):2049–2075, 2013. doi: 10.2514/1.J051895.
- [24] Zhoujie Lyu and Joaquim R. R. A. Martins. Aerodynamic design optimization studies of a blended-wing-body aircraft. *Journal of Aircraft*, 51(5):1604–1617, 2014. doi: 10.2514/1.C032491.
- [25] Ning Qin, Armando Vavalle, Alan Le Moigne, M. Laban, K. Hackett, and P. Weinerfelt. Aerodynamic considerations of blended wing body aircraft. *Progress in Aerospace Sciences*, 40(6):321–343, Aug 2004. doi: 10.1016/j.paerosci.2004.07.001.
- [26] C. Wayne Mastin, Robert E. Smith, Ideen Sadrehaghighi, and Michael R. Wiese. Geometric model for a parametric study of the blended-wing-body airplane. In *14th Applied Aerodynamics Conference*, pages AIAA-96-2416. AIAA, 1996.
- [27] Alexandru Antonau et al. Challenges in realizing 3rd generation multidisciplinary design optimization. *AIMS Applied Computing and Simulation Engineering*, 2025. doi: 10.3934/acse.2025001.
- [28] Yaoran Chen, Zhikun Dong, Jie Su, Yan Wang, Zhaolong Han, Dai Zhou, Yongsheng Zhao, and Yan Bao. Framework of airfoil max lift-to-drag ratio prediction using hybrid feature mining and gaussian process regression. *Energy Conversion and Management*, 243:114339, Sep 2021. doi: 10.1016/j.enconman.2021.114339.
- [29] X. Liu, Q. Zhu, and H. Lu. Modeling multiresponse surfaces for airfoil design with multiple-output-gaussian-process regression. *Journal of Aircraft*, 51(3):740–747, May 2014. doi: 10.2514/1.C032493.
- [30] Ney Rafael Secco and Bento Silva de Mattos. Artificial neural networks to predict aerodynamic coefficients of transport airplanes. *Aircraft Engineering and Aerospace Technology*, 89(2):211–230, Mar 2017. doi: 10.1108/AEAT-06-2015-0151.
- [31] Ana Garcia Garriga, Laura Mainini, and Sangeeth Saagar Ponnusamy. A machine learning enabled multi-fidelity platform for the integrated design of aircraft systems. *Journal of Mechanical Design*, 141(12):121405, 2019.
- [32] Qian Chen, Mohamed Elrefaei, Angela Dai, and Faez Ahmed. Tripnet: Learning large-scale high-fidelity 3d car aerodynamics with triplane networks. *arXiv preprint arXiv:2503.17400*, 2025.
- [33] Charles R. Qi, Hao Su, Kaichun Mo, and Leonidas J. Guibas. Pointnet: Deep learning on point sets for 3d classification and segmentation. In *Proceedings of the IEEE Conference on Computer Vision and Pattern Recognition (CVPR)*, pages 652–660. IEEE, 2017. doi: 10.1109/CVPR.2017.16.
- [34] William L. Hamilton, Rex Ying, and Jure Leskovec. Inductive representation learning on large graphs. In *Advances in Neural Information Processing Systems (NeurIPS)*, pages 1025–1035, 2017.
- [35] Hongyang Gao and Shuiwang Ji. Graph u-nets. In *Proceedings of the 36th International Conference on Machine Learning (ICML)*, 2019.
- [36] Zhongkai Hao, Zhengyi Wang, Hang Su, Chengyang Ying, Yinpeng Dong, Songming Liu, Ze Cheng, Jian Song, and Jun Zhu. Gnot: A general neural operator transformer for operator learning, 2023.
- [37] Haixu Wu, Huakun Luo, Haowen Wang, Jianmin Wang, and Mingsheng Long. Transolver: A fast transformer solver for pdes on general geometries. In *International Conference on Machine Learning*, 2024.
- [38] Ethan Perez, Florian Strub, Harm de Vries, Vincent Dumoulin, and Aaron Courville. FiLM: Visual reasoning with a general conditioning layer. In *Proceedings of the AAAI Conference on Artificial Intelligence*, volume 32, pages 3942–3951, Apr 2018.
- [39] Rohan S. Sharma and Serhat Hosder. Mission-driven inverse design of blended wing body aircraft with machine learning. *Aerospace*, 11(2):137, Feb 2024. doi: 10.3390/aerospace11020137.
- [40] Giovanni Catalani, Siddhant Agarwal, Xavier Bertrand, Frédéric Tost, Michael Bauerheim, and Joseph Morlier. Neural fields for rapid aircraft aerodynamics simulations. *Scientific Reports*, 14(1):25496, Oct 2024. doi: 10.1038/s41598-024-32213-z.
- [41] Zhen Wei, Edouard Dufour, Colin Pelletier, Michaël Bauerheim, and Pascal Fua. Diffairfoil: An efficient novel airfoil sampler based on latent space diffusion model for aerodynamic shape optimization. In *AIAA AVIATION Forum*, 2024. doi: 10.2514/6.2024-3755.
- [42] Reid Graves and Amir Barati Farimani. Airfoil diffusion: Denoising diffusion model for conditional airfoil generation, 2024.
- [43] Jiahao Lin, Shusheng Chen, Shiyi Jin, Quanfeng Jiang, Muliang Jia, and Dong Li. Multi-point aerodynamic inverse design of flying wing using the conditional diffusion model. *Physics of Fluids*, 37(7):077116, 2025. doi: 10.1063/5.0271723.
- [44] Nicholas Sung, Zhiyao Liu, Peishan Wang, and Faez Ahmed. Cooling-guided diffusion model for battery cell arrangement. In *Proceedings of the ASME 2024 International Design Engineering Technical Conferences and Computers and Information in Engineering Conference*, page V03AT03A009, Washington, DC, USA, August 2024. ASME. doi: 10.1115/DETC2024-143373. Volume 3A: 50th Design Automation Conference (DAC). August 25–28, 2024.
- [45] Jeffrey Trac-Pho. Conceptual design of a blended wing body airliner. Master’s thesis, San José State University, San Jose, California, December 2022. Available at <https://www.sjsu.edu/ae/docs/project-thesis/Jeffrey.Trac-Pho-F22.pdf>.

- [46] Robert A. McDonald and James R. Gloudemans. Open vehicle sketch pad: An open source parametric geometry and analysis tool for conceptual aircraft design. In *AIAA SciTech 2022 Forum*, San Diego, CA, Jan 2022. doi: 10.2514/6.2022-0004. AIAA Paper 2022-0004.
- [47] Cadence Design Systems, Inc. Fidelity pointwise (version 2024.1). <https://www.cfd-technologies.co.uk/fidelity-pointwise>, March 2025. Accessed: 2025-03-12.
- [48] William K. Anderson, Robert T. Biedron, Jan-Reneé Carlson, Joseph M. Derlaga, Boris Diskin, Cameron T. Druyor Jr, Peter A. Gnoffo, Dana P. Hammond, Kevin E. Jacobson, William T. Jones, and William L. Kleb. *FUN3D Manual: 14.1*. NASA Langley Research Center, Hampton, VA, 2024. NASA Technical Manual.
- [49] John D. Anderson. *Fundamentals of aerodynamics*. McGraw-Hill series in aeronautical and aerospace engineering. McGraw Hill LLC, New York, NY, seventh edition. edition, 2024. URL <https://ebookcentral.proquest.com/lib/mit/detail.action?docID=7192797>.
- [50] Will Schroeder, Ken Martin, and Bill Lorensen. *The Visualization Toolkit (4th ed.)*. Kitware, 2006. ISBN 978-1-930934-19-1.
- [51] Albert Reuther, Jeremy Kepner, Chansup Byun, Siddharth Samsi, William Arcand, David Bestor, Bill Bergeron, Vijay Gadepally, Michael Houle, Matthew Hubbell, Michael Jones, Anna Klein, Lauren Milechin, Julia Mullen, Andrew Prout, Antonio Rosa, Charles Yee, and Peter Michaleas. Interactive supercomputing on 40,000 cores for machine learning and data analysis. In *2018 IEEE High Performance Extreme Computing Conference (HPEC)*, pages 1–6, Waltham, MA, Sep 2018. IEEE. doi: 10.1109/HPEC.2018.8547629.
- [52] Florent Bonnet, Jocelyn Ahmed Mazari, Paola Cinnella, and Patrick Gallinari. Airfrans: High fidelity computational fluid dynamics dataset for approximating reynolds-averaged navier–stokes solutions. In *NeurIPS 2022 Datasets and Benchmarks Track*, 2022. URL <https://openreview.net/forum?id=HEJ2K8QLHwJ>.
- [53] Faez Ahmed, Cyril Picard, Wei Chen, Christopher McComb, Pingfeng Wang, Ikjin Lee, Tino Stankovic, Douglas Allaire, and Stefan Menzel. Special issue: Design by data: Cultivating datasets for engineering design. *Journal of Mechanical Design*, 147(4):040301, 02 2025. ISSN 1050-0472. doi: 10.1115/1.4067871. URL <https://doi.org/10.1115/1.4067871>.
- [54] Tsinghua University Machine Learning Group (THUML). Neural-solver-library: A library for advanced neural pde solvers. <https://github.com/thuml/Neural-Solver-Library>, 2025. Last accessed: September 29, 2025.

A Appendix

A.1 Supplementary Dataset Distributions

Figures 8 and 9 report the distributions of the sampled variables. Figure 8 shows histograms of the normalized planform parameters within the bounds of Table 3. Figure 9 shows the flight-condition marginals (altitude, Mach, $\log_{10} Re_L$, and α).

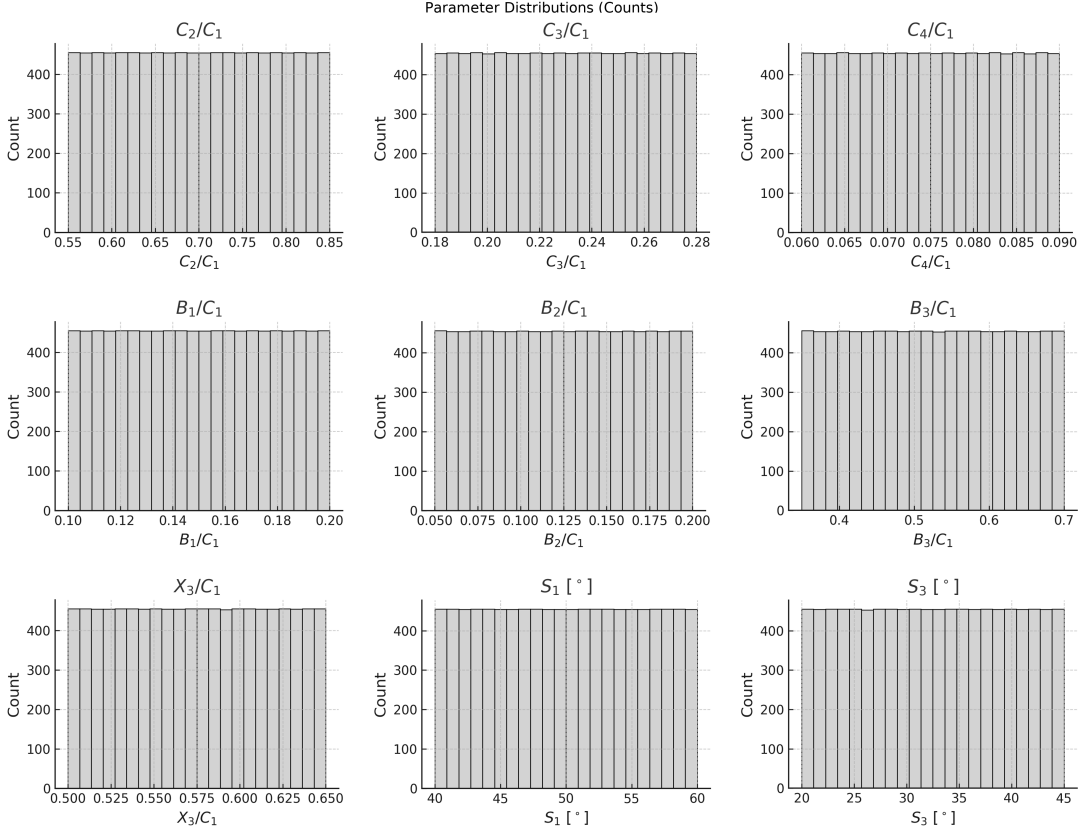


Figure 8: Distributions (counts) of normalized planform parameters for BlendedNet++. Each panel shows the marginal histogram of a single parameter within the bounds listed in Table 3.

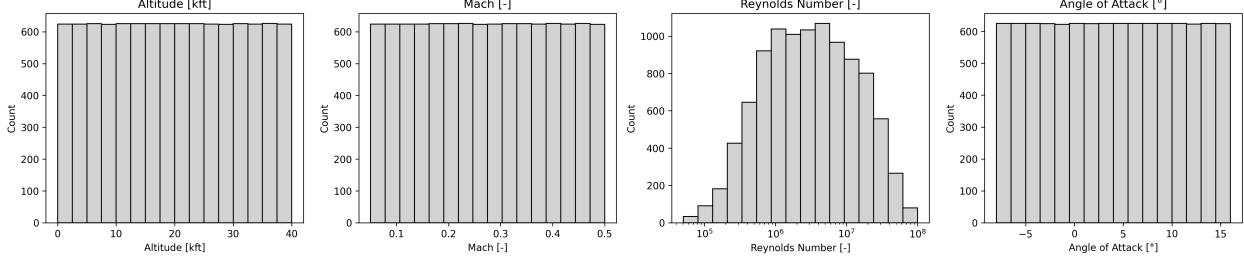


Figure 9: Flight-condition distributions for BlendedNet++: altitude, Mach number, Reynolds number (log-scaled on the horizontal axis), and angle of attack.

A.2 BlendedNet vs. BlendedNet++ Comparison

A t-SNE embedding of the latent space learned by a PointNet autoencoder, trained on both datasets, is shown in Figure 10, where each point corresponds to a geometry and is colored by dataset.

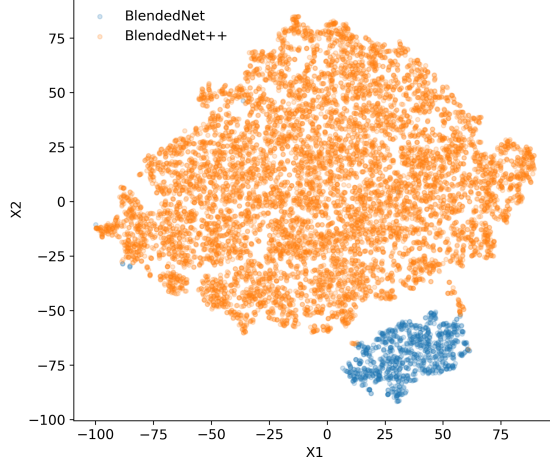


Figure 10: t-SNE of PointNet autoencoder latent space for BlendedNet and BlendedNet++. Each point is one geometry.

We also visualize the flight-condition distribution to show sampling coverage across Altitude, Reynolds Number, Mach Number and Angle of Attack (Figure 11).

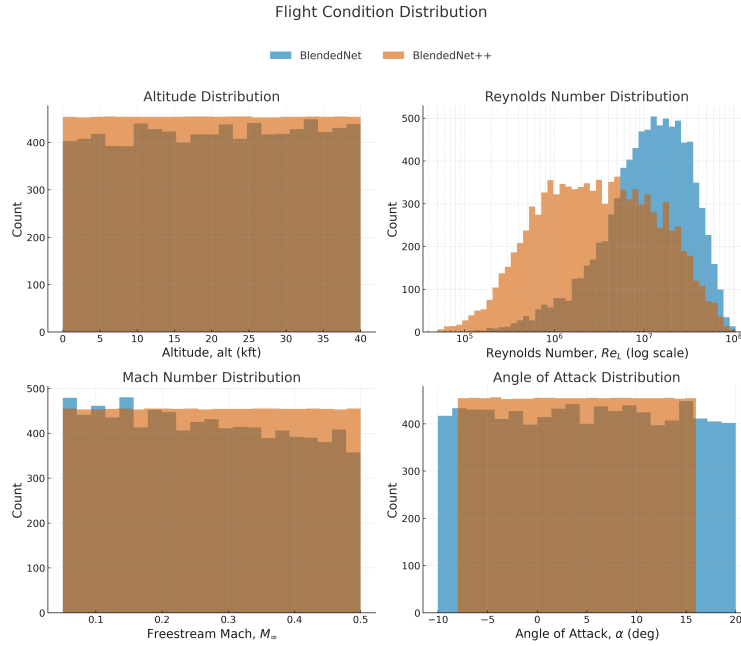
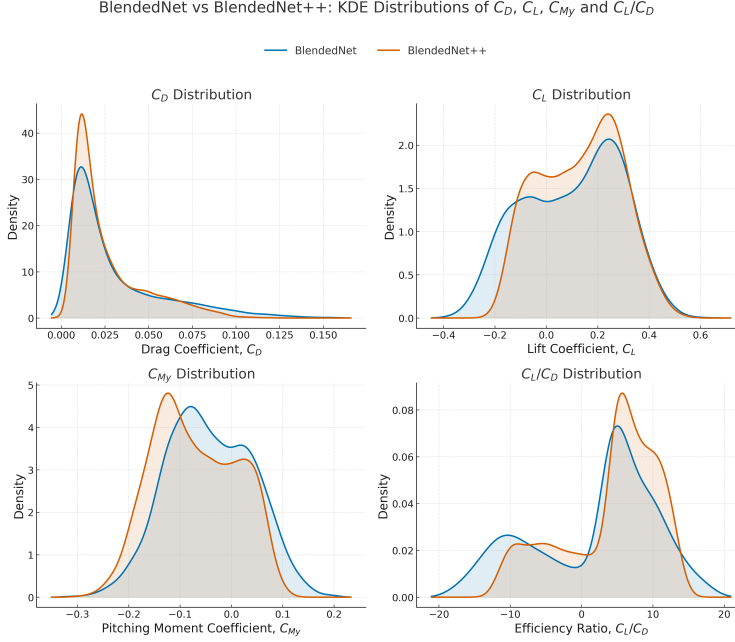


Figure 11: Distribution of flight conditions using Altitude, Reynolds Number, Mach Number and Angle of Attack.

Finally, Figure 12 compares the distributions of the aerodynamic coefficients C_D , C_L , C_M , and the efficiency ratio C_L/C_D .

Figure 12: Distributions of C_D , C_L , C_{M_y} , and efficiency C_L/C_D for BlendedNet vs. BlendedNet++.

A.3 Forward Surrogate Training Details

A.3.1 Common preprocessing

We follow the default settings in the *NeuralSolver* library [54]. The 3 condition inputs ($\log_{10} Re_L$, M_∞ , α) are standardized to have zero mean and unit variance. Each output channel (C_p , C_{f_x} , C_{f_z}) is z scored independently. During training we draw a uniform subsample of roughly 8×10^3 surface points per geometry so that batches remain consistent across meshes. During evaluation we use the full surface without subsampling. The training loss is a single mean squared error computed over all points and over the 3 output channels with equal weight.

A.3.2 Optimization and schedules

All PointNet, Transolver, and GNOT models are trained with AdamW. The initial learning rate is 5×10^{-4} . The weight decay is 1×10^{-5} . We use a One Cycle learning rate schedule that rises during the first third of training and then anneals for the remaining steps. We do not apply gradient clipping. Mixed precision remains at the library default. We save periodic checkpoints. For test metrics we evaluate both the checkpoint with the best validation loss and the final epoch checkpoint and we report the better of the two for each model. Across all forward surrogate models, we train on a single NVIDIA A100 GPU with early stopping based on validation loss (50-epoch warmup and a patience of 30 epochs), and we cap the wall-clock training budget at approximately 24 hours per model.

A.3.3 Model-specific settings

FiLMNet (ours). FiLMNet is a coordinate MLP whose hidden layers are modulated by a small hypernetwork that maps the condition vector to per layer scale and shift. The per point input is a 6 dimensional coordinate made of 3 normalized spatial coordinates and the local surface normal. The conditioning vector has 12 scalars that combine the standardized flight inputs with the standardized planform parameters. The modulation network produces the FiLM scales and shifts and the base MLP has 4 hidden layers of width 256 followed by 3 extra non modulated layers before the output head. We predict 3 channels at each surface point namely C_p , C_{f_x} , and C_{f_z} . In training we keep the normalization statistics fixed from the training split. We optimize with Adam using a constant learning rate of 5×10^{-4} and a batch size of 64, following the shared early-stopping schedule described above.

PointNet (NeuralSolver). The PointNet backbone is a lightweight stack of 8 multilayer perceptron blocks with a narrow hidden width. The network applies the same small per point MLP and then aggregates. Each point sees its 3 dimensional coordinates together with a compact feature vector that includes the broadcasted condition and planform scalars and the local surface normal. The default feature dimension is 15 which covers these quantities. In our runs the hidden width is 32 across the 8 layers. This configuration is intended as a strong and fast baseline rather than a heavily tuned model. The batch size is 64, and training follows the shared optimization and early-stopping schedule.

Transolver (NeuralSolver). Transolver augments per point features with physics aware tokenization and attention. We use the default medium capacity. The depth is 8 transformer style blocks. The hidden width is 256 per block. There are 8 attention heads. We keep the library default tokenization settings. This includes the number of slices which is 32 and the reference neighborhood size which is 8. The attention implementation follows the default Nyström style variant. The activation function is GELU. This setting balances global context with good runtime. The batch size is 64, and training uses the same early-stopping schedule and 24-hour per-model budget as the other forward surrogates.

GNOT (NeuralSolver). GNOT is a transformer style operator on graphs that captures long range interactions on the surface. We match the general capacity used for Transolver. The network depth is again about 8 blocks with a hidden width of 256 units and 8 attention heads. We keep the operator and attention hyperparameters at their library defaults. Inputs mirror the Transolver setup. Each point uses its coordinates its local normal and the same compact feature vector of broadcasted scalars. The batch size is 64, with training controlled by the shared early-stopping schedule and 24-hour budget.

GraphSAGE (NeuralSolver). GraphSAGE operates on dynamic k -NN graphs built from the surface point cloud each iteration. We use three message-passing layers with a hidden width of 128, mean aggregation, and residual connections. Each point ingests its 3D coordinates and local surface normal together with a compact broadcasted feature vector of flight and planform scalars. Layers apply ReLU activations, layer normalization, and dropout ($p = 0.2$). Graphs are formed with $k = 15$ neighbors and rebuilt per batch. A light pointwise MLP maps the final node embeddings to the three output channels C_p , C_{f_x} , and C_{f_z} . The batch size is 32, and we used the Adam optimizer with a learning rate of 5×10^{-4} under the shared early-stopping schedule.

GraphUNet (NeuralSolver). GraphUNet follows a U-Net style encoder–decoder on graphs with five resolution levels. We use SAGE convolutions with a hidden width of 128, random pooling at ratio 0.5 across the down path, and symmetric skip connections in the up path. Edges are derived from a dynamic k -NN graph with $k = 20$. The batch size is 32. We used the Adam optimizer with a learning rate of 1×10^{-3} , combined with a ReduceLROnPlateau scheduler for adaptive learning rate decay, and the same early-stopping criterion and 24-hour budget as the other forward surrogates.

Across PointNet, Transolver, GraphSAGE, GraphUNet, and GNOT we deliberately adopt the off the shelf NeuralSolver defaults. FiLMNet follows the same preprocessing and data split. We keep optimizer choice schedule and model capacity comparable. This design lets the comparison focus on architectural inductive bias rather than hyperparameter tuning. For test metrics across all model, we again compare the checkpoint with the best validation loss and the final epoch checkpoint and we report the better result.

A.4 Inverse Design: Optimization & Diffusion Details

A.4.1 Conditional diffusion configuration

We train a conditional denoising model that maps a noisy geometry vector to new planform parameters under a fixed condition vector. The condition vector contains altitude in kft, $\log_{10} Re_L$, free-stream Mach number M_∞ , angle of attack in degrees, and the target lift to drag ratio. We standardize the condition entries to zero mean and unit variance. Geometry is the nine-dimensional planform vector p and is mapped to the interval $[-1, 1]$ using a symmetric min–max scaler that is fitted on the training split. Timesteps use sinusoidal positional embeddings. The denoiser is a residual multilayer perceptron with a hidden width of 512 and depth 6 residual blocks (ResMLP). Each block applies LayerNorm and SILU activations in the residual MLP. We used a cosine noise schedule for β_t and a standard reparameterization in the reverse process. We optimize with AdamW and match the learning rate, batch size, and number of epochs used for the forward surrogates so that the conditioning statistics remain consistent during training. At sampling time we draw one hundred independent Gaussian noise seeds per condition and run the full reverse process to produce one hundred sample geometries.

A.4.2 Projected gradient descent

We implement a simple projected gradient method that operates in the standardized planform space. The objective is the squared error between the surrogate prediction of L/D and the target value. Gradients come from the differentiable surrogate. Each update takes a step along the negative gradient and then projects back into the feasible box by clipping each coordinate to its bound. For the multi-start baseline we initialize one hundred seeds uniformly within the box and run a long schedule of updates. For the hybrid we initialize from the one hundred diffusion samples and run a shorter schedule. In both cases we keep the step size fixed after a single validation sweep and we use the same setting for all test conditions. We report the best candidate across the one hundred trajectories for each condition. As summarized in Table 9, the Opt baseline uses one thousand projected steps per condition, and the CDM→Opt hybrid uses two hundred projected steps per condition.

A.4.3 Projected gradient descent for the baseline optimizer

For the gradient baseline we optimize a parametric L/D surrogate with projected gradient descent in the normalized feature space. For each test condition we draw 100 random seeds inside the box of valid planforms and we hold the flight condition features fixed to the row values while optimizing geometry. We run 1000 gradient steps with a learning rate of 0.05 on the normalized variables. We use plain SGD on the decision tensor without momentum. After every step we project by mapping the normalized vector back to raw units, clipping geometry to the physical box, fixing the condition coordinates, and mapping to normalized space again.